Effects of Heat Treatment on Corrosion and Wear Behaviors of Mg-6Gd-2Zn-0.4Zr Alloy in Simulated Body Fluid

Li Zhao, Wei Chen, Jianwei Dai, Zhangzhong Wang, and Xiaobo Zhang

Mg-6Gd-2Zn-0.4Zr (wt.%, GZ62K) alloy was processed by solution treatment under different temperatures. The microstructure, hardness, corrosion and wear behaviors in simulated body fluid (SBF) have been studied. The results indicate that the $(Mg, Zn)_3Gd$ phase decreases, the precipitated phases gradually increase, and the long-period stacking ordered structure disappears with the increase of solution temperature. The alloy has better corrosion resistance after solution treatment, and that solution treated at 490 °C for 12 h shows the best corrosion resistance. The friction coefficient of the alloy under dry sliding condition decreases slightly, but the mass loss increases with increasing the solution temperature. The alloy solution treated at 460 °C for 12 h exhibits the lowest friction coefficient and mass loss in SBF, and it also has the best wear resistance under dry sliding condition.

1. Introduction

Magnesium (Mg) alloys have played increasingly important roles in metal-implanted materials due to some desirable properties, such as good biocompatibility, mechanical properties and biodegradation (Ref 1, 2). First of all, Mg is a nutritive element and the fourth most abundant cation in human body. It is found that Mg can accelerate the growth of the bone tissue by promoting bioactivity, which is of great significance to physical body (Ref 3-5). Secondly, compared with the traditional titanium alloys and stainless steels, the elasticity modulus of Mg alloys is much closer to that of the human bone, which avoids the stress shielding effect (Ref 6). Additionally, biomedical Mg alloys can degrade completely in human body after healing the disease due to their low corrosion potential (Ref 7, 8). Therefore, as bone-implanted materials, the biodegradation of Mg alloys can make patients avoid the secondary operation, alleviating the suffering and economic burden of the patients.

Recently, great progress on Mg alloys has been made for biomedical applications (Ref 9-12). Zhang et al. (Ref 9) implanted a pin made of ultra-pure Mg into the intact distal femur in rats and found the formation of new bone at peripheral cortical sites, accompanied with substantial increase of neuronal calcitonin gene-related polypeptide-a (CGRP) in ratios.

They created an intramedullary nail containing Mg to promote the fracture repair in rats using ovariectomy-induced osteoporosis, and the results revealed that Mg played an important role in promoting CGRP-mediated osteogenic differentiation. Haude et al. (Ref 10) operated second-generation drug-eluting absorbable metal scaffold in 123 patients and found that this implantation was feasible in de-novo coronary lesions, indicating this absorbable metal scaffold could be a novel alternative to treat obstructive coronary disease. These positive results make the biodegradable Mg alloys promising for biomedical applications. For bone implant applications, the material serves in human body under corrosive condition and suffers corrosion and friction simultaneously. Several studies have shown that the implants induce fretting friction and wear while being implanted into bones, causing failure of the clinical surgery (Ref 13-15). However, few researches have focused on friction and wear behaviors of Mg alloys in simulated body fluid (SBF) for biomedical applications. Therefore, further study needs to be carried out on wear behavior in SBF.

Heat treatment has a great impact on wear behavior. Cao et al.. studied the dry tribological behavior of as-cast and solution-treated Mg-Gd-Zn-Zr alloy and found the solution-treated alloy presented worse wear resistance than the as-cast one because of the decrease of harder β-phase and the formation of plastic X-phase (Ref 16). Zhang et al.. reported the age-treated Mg-Gd-Zn-Zr alloy showed better dry sliding wear resistance under higher applied load than the as-cast one due to significant work hardening (Ref 17). In addition, proper heat treatment plays a positive role in improving corrosion resistance of magnesium alloys (Ref 18-20). This can be attributed to the fact that heat treatment can obviously decrease the second phase and promote the precipitated phase distributed homogeneously, which is good for reducing galvanic corrosion, resulting in low corrosion rate and uniform corrosion mode (Ref 21).

Considering the bone fixture application of Mg alloys, it is necessary to illustrate both corrosion and wear behaviors in SBF. Our previous work suggested that the cell toxicity of Mg-

Li Zhao, Wei Chen, Jianwei Dai, Zhangzhong Wang, and **Xiaobo Zhang**, School of Materials Science and Engineering, Nanjing Institute of Technology, Nanjing 211167, China; and Jiangsu Key Laboratory of Advanced Structural Materials and Application Technology, Nanjing 211167, China. Contact e-mail: xbxbzhang2003@163.com.

11.3Gd-2.5Zn-0.6Zr could meet the requirements of cell toxicity as biomaterials (Ref 22). It has been also reported that Gd, Zn and Zr elements are potential candidates for alloying elements in Mg alloys due to their acceptable cell toxicity (Ref 23-25). Therefore, in this work, Mg-6Gd-2Zn-0.4Zr alloy, a promising biodegradable Mg alloy according to our previous study (Ref 26), was chosen as the researched subject, and the effects of heat treatment on corrosion and wear behaviors in SBF have been studied.

2. Experimental

The Mg-6Gd-2Zn-0.4Zr (wt.% GZ62K) alloys were prepared by gravity casting (Ref 26). And the ingots were solution treated at 460, 490, 520 and 550 °C for 12 h, respectively, under a protective atmosphere, followed by water quenching at room temperature. The alloys under different conditions were denoted as F, T4-460, T4-490, T4-520 and T4-550, respectively. Specimens with a dimension of Ø 14 mm × 3.5 mm for the corrosion test and a dimension of 10 mm × 10 mm × 6 mm for the friction and wear tests were cut by wire cut electrical discharge machining. After grinding by SiC paper, the samples were polished with diamond paste, cleaned by anhydrous alcohol ultrasonically, and dried with warm air finally. The samples were soaked in the 4% nitric acid alcohol solution and cleaned in anhydrous ethanol. The micrographs of the samples were captured by using a scanning electron microscope (SEM) coupled with an energy-dispersive spectrometer (EDS). The hardness of the specimens was measured by Vicker's micro-hardness testing.

Corrosion test was conducted by immersing the specimens in SBF at 37 °C for 120 h to calculate the corrosion rate (Ref 27). The ratio of SBF volume to surface area is 60 ml: 1 cm^2, and the SBF was renewed every 24 h. After being immersed for 120 h, the specimens were removed from the SBF and dried. The morphologies of corrosion products were observed by SEM, and then, the specimens were placed in a boiling acid solution of 200 g/L CrO$_3$ and 10 g/L AgNO$_3$ in distilled water for 5 min to remove the corrosion products (Ref 27). The mass loss of the specimens before and after immersion test was recorded. The polarization curves were measured in SBF at 37 °C using a standard three-electrode glass cell with a scan rate of 1 mV/s. The platinum sheet, the saturated calomel electrode and the specimen served as the counter electrode, the reference electrode and the working electrode, respectively.

The experiment of friction and wear was carried out using a ball-on-disk friction and wear testing machine under both dry and SBF sliding conditions, respectively. Grinding part is stainless steel ball. The sliding speed is 20 mm/s, the applied load is 20 N, and the test lasts for 60 min. The data about the friction coefficient versus the sliding time were recorded by computer automatically. After the friction and wear test, the samples were cleaned ultrasonically in anhydrous ethanol and then weighed by analytical balance. The worn morphologies of the worn surface were analyzed by SEM. The corrosion products on the surface of the worn specimens were removed by the same way as the corrosion test. The mass of the specimens was weighted again to calculate the total mass loss caused by wear and corrosion. In addition, after tribological test, the wear debris was collected from the dry sliding

specimen and SBF sliding specimen after drying with cold wind for EDS analysis.

3. Results and Discussion

3.1 Microstructure and Hardness

SEM micrographs of the GZ62K alloy at different conditions are shown in Fig. 1. The microstructure of the as-cast GZ62K alloy is mainly composed of α-Mg matrix, eutectic phase (α + β) at grain boundaries and LPSO structure throughout some whole matrix grains, as shown in Fig. 1(a). In contrast, the microstructure after solution treatment consists of α-Mg matrix and eutectic phase around grain boundaries, and the lamellar LPSO structure cannot be observed. With the increase of solution temperature, the bright eutectic phase gradually decreases and becomes discontinuous. Moreover, numerous tiny particles which are circled in Fig. 1(c) precipitated, and their amount increases with increasing the solution temperature, as shown in Fig. 1(b), (c), (d), and (e).

According to our previous report (Ref 26), the bright β phase is (Mg, Zn)$_3$Gd. With the increase of heat treatment temperature, the amount of the β phase with higher Gd and Zn decreases because more and more Gd and Zn atoms dissolve into α-Mg matrix. The LPSO structure disappears after solution treatment, which is well consistent with the result found by Rong et al. (Ref 28), because Zr element consumes some Zn during solution treatment, and thus, hinders the formation of LPSO structure within α-Mg matrix. More Zr precipitates from α-Mg matrix with the increase of the heat temperature, leading to more volume fraction of the precipitates and disappearance of the LPSO structure.

Further magnified microstructure of the T4-550 alloy is shown in Fig. 2, and the chemical compositions of different areas marked in Fig. 2 are listed in Table 1. The chemical compositions of area A (α-Mg matrix) are close to the nominal composition of the alloy. Area B with bright needle-like precipitates has a higher concentration of Zr compared to the α-Mg matrix, as well as Gd and Zn, showing that the precipitated phase is Zr-rich phase which is corresponding to our previous reports (Ref 26). Area C located at grain boundary has the highest concentration of Gd and Zn, and the lowest concentration of Zr. The bright block phase discontinuously distributed along the grain boundaries is still referred to be residual (Mg, Zn)$_3$Gd phase (Ref 26).

Figure 3 shows the Vicker's microhardness of the GZ62K alloy under different conditions. It shows that the hardness of the T4-460 alloy is a little lower than the F alloy. The eutectic phase after solution treated at 460 °C was not reduced apparently as shown in Fig. 1(b). So the solution strengthening is not obvious. Moreover, it is known that the hardness of the LPSO structure in Mg-Gd-Zn alloy is higher than that of the α-Mg matrix (Ref 29). Consequently, the disappearance of the LPSO structure is responsible for the hardness reduction of the T4-460 alloy as compared to the F alloy. The hardness of the alloy after solution treatment increases slightly with the increment of solution temperature. As shown in Fig. 1(b), (c), (d), and (e), the eutectic phase decreases and the precipitates increase with the increase of solution temperature, and thus, solution strengthening and precipitation strengthening lead to the hardness improvement.
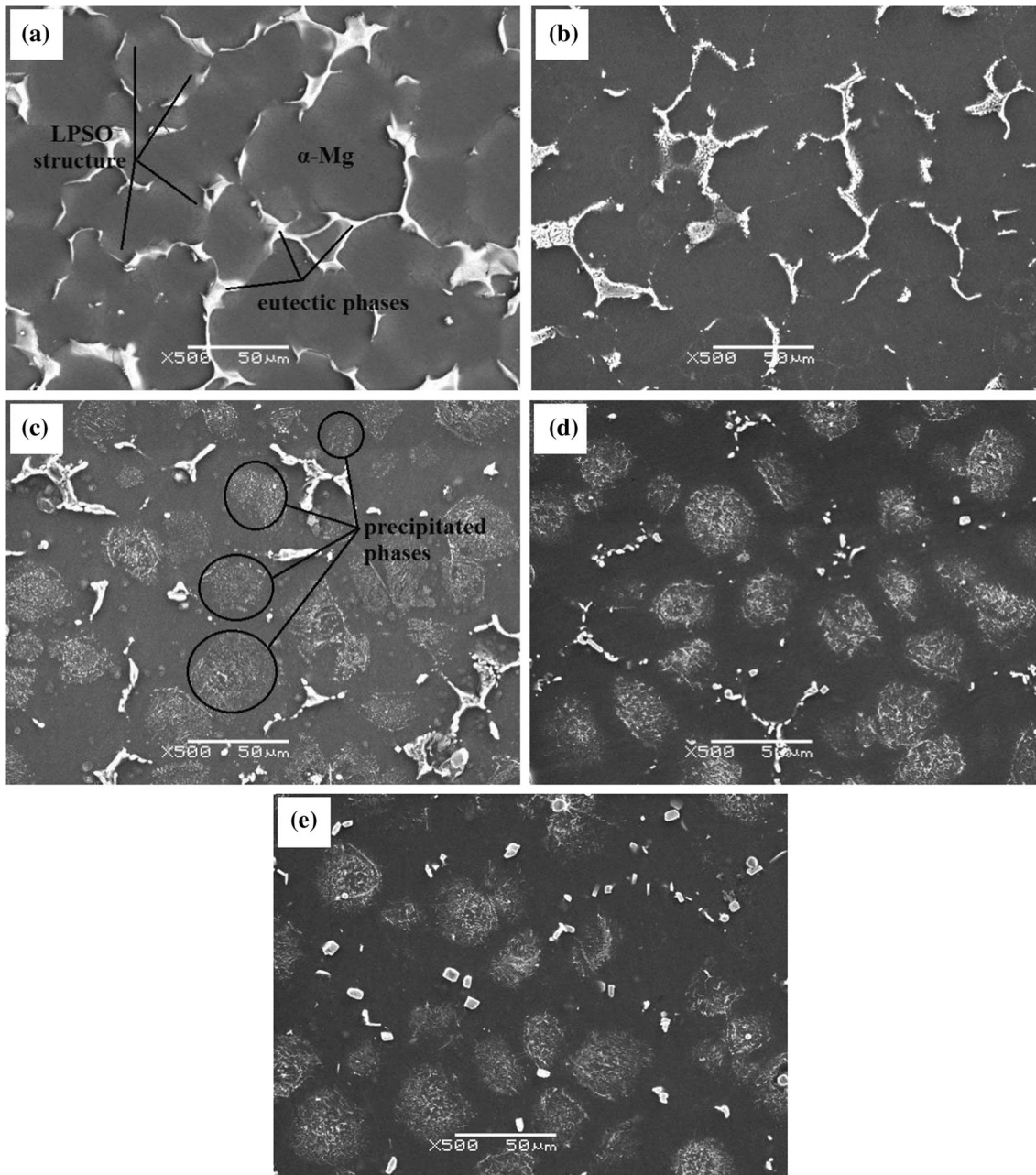
Fig. 1 SEM images of the GZ62K alloys (a) F, (b) T4-460, (c) T4-490, (d) T4-520, (e) T4-550

3.2 Corrosion Properties

The corrosion rates of the alloys after immersion in SBF for 120 h are plotted in Fig. 4. The corrosion resistance is improved apparently from 23 to 44% after solution treatment. The corrosion rate firstly decreases and then increases with the increase of the solution temperature. It is found that the lowest corrosion rate is achieved for the T4-490 alloy, which is only 56% of the as-cast one. Consequently, the corrosion morphologies of the F alloy with the highest corrosion rate and the T4-490 alloy with the lowest corrosion rate were compared after immersion in SBF for 120 h, as shown in Fig. 5. More corrosion products aggregate on the surface of the as-cast alloy, while the eutectic phase outline on the surface of sample is still visible as marked in Fig. 5(b), indicating much less corrosion.

Figure 6 shows the potentiodynamic polarization curves of the GZ62K alloy under different conditions. The corrosion potential and corrosion current density of the alloy obtained by Tafel extrapolation from the cathodic curves are listed in Table 2. It shows that all the specimens after solution treatment have lower corrosion potential (E_{corr}) than the as-cast one, suggesting an easier corrosion trend from the view of corrosion thermodynamics. However, thermodynamic stability is not considered to be the key issue in the determination of Mg alloy corrosion, with the kinetics of corrosion determining the ultimate corrosion rate, as potential difference does not necessarily translate to kinetic effects (Ref 30). This means that the corrosion rate of the alloy is actually determined by corrosion current density from the view of corrosion kinetics

but not by the corrosion potential. According to Tafel extrapolation, the current densities (I_{corr}) of the specimens after solution treatment are lower than that of the as-cast one, indicating that the corrosion resistance of the alloy after solution treatment is better than that of the as-cast alloy, which is well consistent with the immersion result shown in Fig. 4. The Mg alloys with nobler corrosion potential but higher current density were often reported in Mg alloys, such as Mg-Al (Ref 31), Mg-Zn-Y (Ref 32) and coated Mg-Sr alloys (Ref 33). Nevertheless, the I_{corr} of the T4-490 is the highest among the solution-treated alloys, which is different from the corrosion rates acquired by immersion mass loss test. This can be attributed to the different tests between immersion and polarization. Immersion test is an effective way to measure the average corrosion rate in a long term, while the polarization test is to obtain instant corrosion rate (Ref 34, 35). The immersion test is suggested to be more reliable than the polarization test for measuring corrosion rates of Mg alloys (Ref 34, 35).

The eutectic phase and LPSO structure apparently impact the corrosion resistance of Mg-Gd-Zn(-Zr) alloys (Ref 36-38). When the volume fraction of the eutectic phase is relatively low and the LPSO structure distributes at the outer edges of the matrix grains, the alloy exhibits uniform corrosion and good corrosion resistance because the LPSO structure with moderate Gd and Zn concentration acts as a bridge between the eutectic phase and matrix (Ref 37). Contrarily, when the volume fraction of the eutectic phase is high and the LPSO locates throughout whole matrix grains, the bridge effect disappears, and more eutectic phase results in faster and more localized corrosion (Ref 26). Consequently, the highest corrosion rate of the as-cast alloy is mainly caused by the LPSO structure located throughout whole matrix grains and more eutectic phase. After solution treatment, mor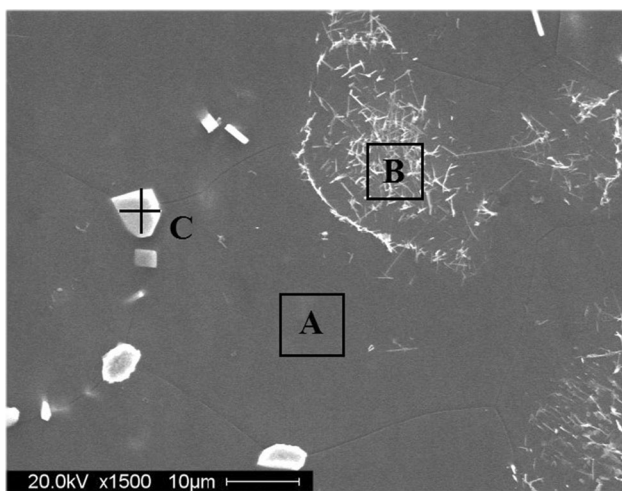e eutectic phase dissolves into the matrix which leads to the decrease of corrosion. When the solution temperature is over 490 °C, the precipitated phase increases, and the Zr-rich precipitates can lead to galvanic corrosion due to their higher corrosion potential compared with the matrix (Ref 26).

3.3 Friction and Wear Behaviors

The friction coefficient of the alloy versus the sliding time is plotted in Fig. 7. The T4-460 has the highest friction coefficient under dry sliding condition, followed by the T4-490, F, T4-520 and T4-550, but they show only slight difference. The friction
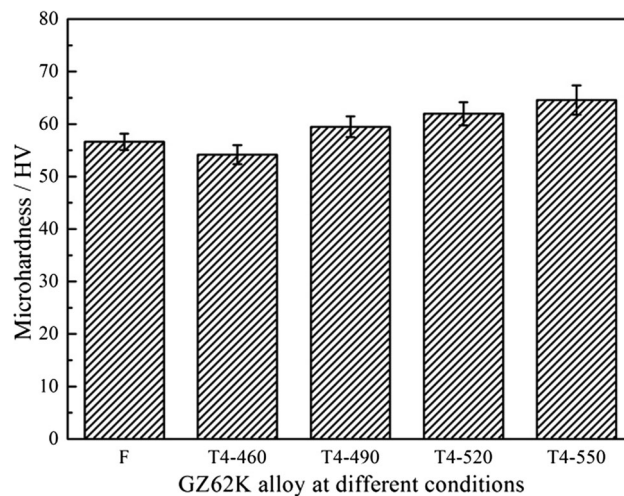

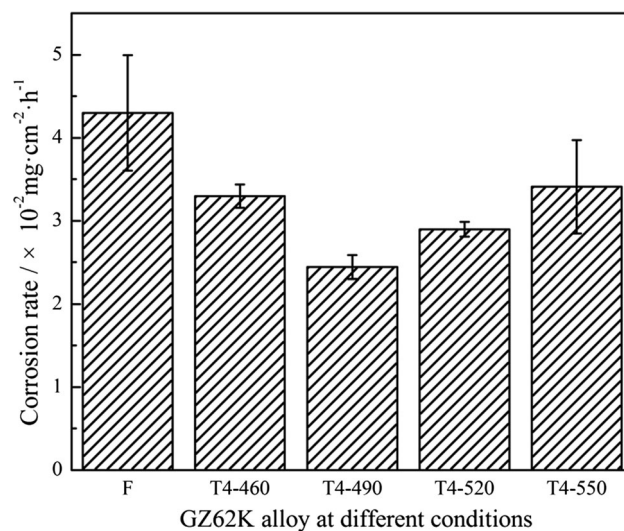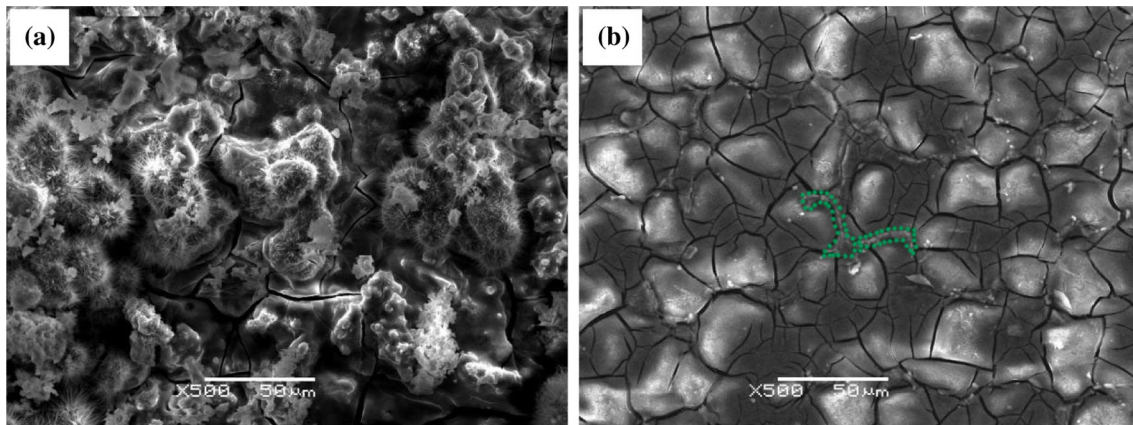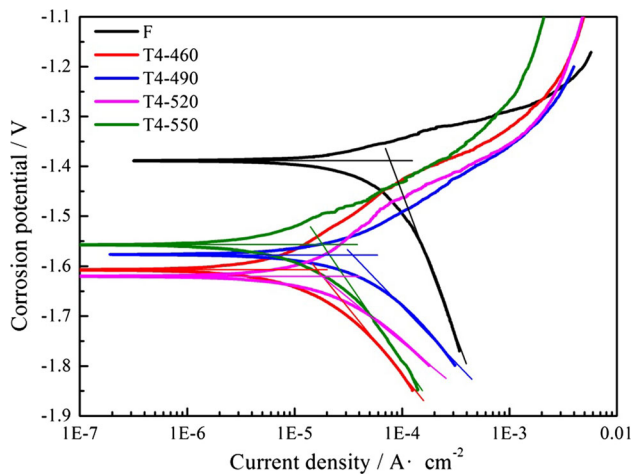Fig. 3 Microhardness of the GZ62K alloys

Fig. 2 Microstructure of the T4-550 alloy

Fig. 4 Corrosion rates of the GZ62K alloys after immersion in SBF for 120 h

Table 1 Chemical composition (mass fraction, %) of the marked areas in Fig. 2

Area	Mg	Gd	Zn	Zr
A	91.20	5.87	1.95	0.98
B	87.27	7.38	2.44	2.91
C	37.64	38.13	24.07	0.16

Fig. 5 Corrosion morphologies of the F (a) and T4-490 (b) after immersion in SBF for 120 h

Fig. 6 Polarization curves of the GZ62K alloys in SBF

Table 2 Electrochemical parameters obtained from cathodic curves in Fig. 6

Alloy	E_{corr}, V	I_{corr}, A cm^{-2}
F	−1.390	7.7×10^{-5}
T4-460	−1.606	1.7×10^{-5}
T4-490	−1.579	3.4×10^{-5}
T4-520	−1.620	1.8×10^{-5}
T4-550	−1.557	1.9×10^{-5}

coefficient decreases apparently in SBF, and that of the T4-460 is the lowest. In addition, the friction curves are much smoother in SBF than dry sliding, indicating a good lubrication caused by SBF.

In general, with the increase of solution treatment temperature, the friction coefficient decreases slightly for the dry sliding. This may attribute to the more reduction of eutectic phase and enhancement of hardness. The friction coefficient is significantly reduced in SBF because of the effective lubrication of SBF. Firstly, SBF can take away the friction heat and thus avoid softening magnesium alloys on account of poor high-temperature soft resistance (Ref 39). Moreover, the removal of wear debris by SBF and the formation of Mg(OH)$_2$ films lessen the surface roughness. Therefore, the friction

coefficient is much lower in SBF than that under dry sliding condition, suggesting a better wear resistance in SBF (Ref 40).

The mass loss of the alloys at different conditions is shown in Fig. 8. During the friction and wear test in SBF, the wear consumes some mass. Contrarily, corrosion products on the surface of the specimen can increase some mass before they are removed. So the negative mass loss is even obtained prior to removing corrosion products. We calculated the mass loss before and after removing corrosion products, and the mass loss of the alloys in SBF after removing the corrosion products represents the total mass loss caused by wear and corrosion. It is clear that the mass loss of dry sliding is much higher than that in SBF before removing corrosion products and a little lower than that after removing corrosion products except for the T4-550 alloy. The mass loss under dry sliding and in SBF increases with increasing solution treatment temperature before the corrosion products are removed, and that in SBF after removing corrosion products increases first and then presents a slight decrease. The total mass loss of the T4-460 alloy is the lowest under both dry and SBF conditions, indicating the best wear resistance.

With the increase of solution treatment temperature, the mass loss increases under dry sliding condition mainly due to the increased precipitated phase. This is opposite to the trend of their friction coefficient and hardness, because the precipitated hard particles probably accelerate the abrasive wear (Ref 17). The mass loss before removing corrosion products formed in SBF is much less than that under dry sliding condition, but it is even a little higher after removing corrosion products compared with that under dry sliding condition (exception for the T4-550 alloy) on account of the corrosion. Nevertheless, which dominates the mass loss is not clear only according to the mass loss results. So the worn surfaces of the F alloy and the T4-460 alloy with the lowest mass loss were observed by SEM and compared, as shown in Fig. 9. According to the size of the worn tracks in Fig. 9, the width of the worn track in Fig. 9(a) is a little wider than that in Fig. 9(c), as well as the length. The same result can be obtained from Fig. 9(b) and (d). These have a good agreement with the mass loss results shown in Fig. 8. Compared with the worn tracks formed in SBF, those formed under dry sliding are much rougher, which is consistent with the friction coefficient.

Moreover, the volume of the worn tracks formed in SBF is approximate 1/30 of that formed under dry sliding according to the width, length and depth of the worn tracks shown in Fig. 9.
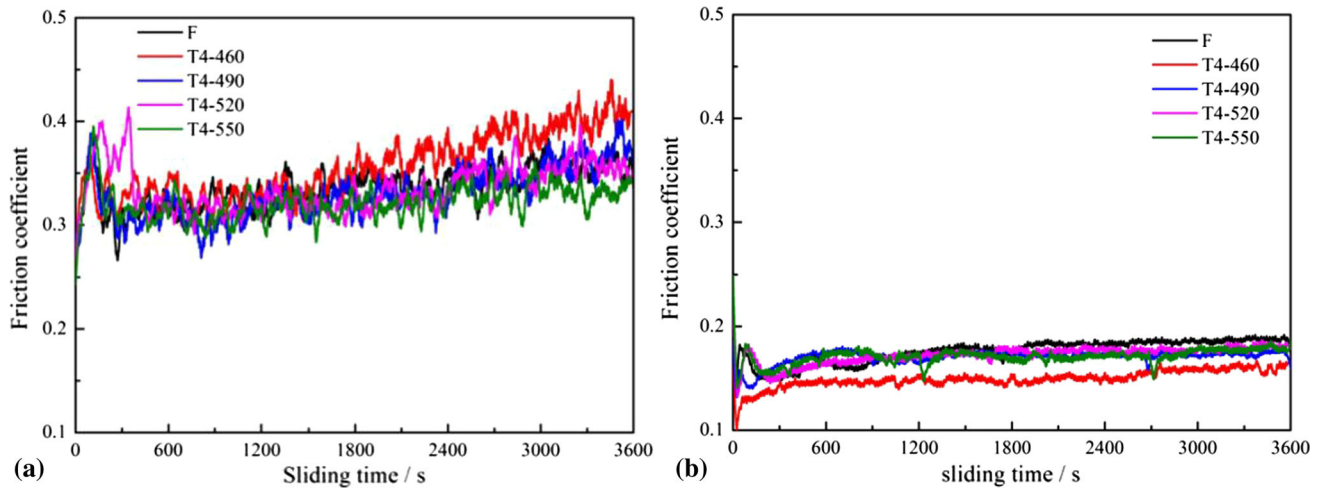
Fig. 7 Friction coefficient curves of the GZ62K alloys under dry sliding (a) and in SBF (b)
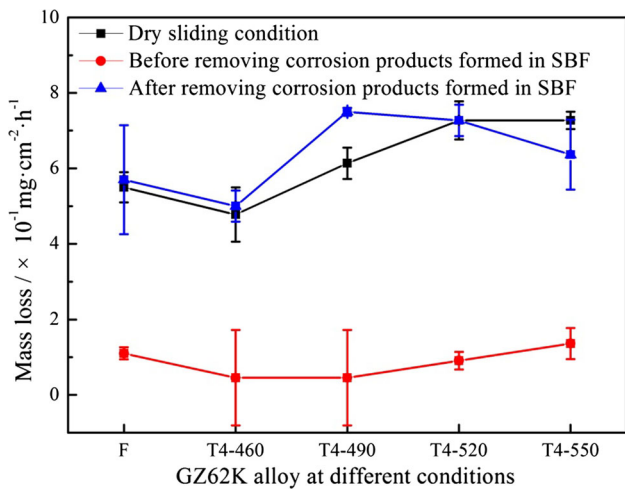

Fig. 8 Mass loss of the GZ62K alloys under dry and SBF sliding conditions

This means that the mass loss caused by wear in SBF is only 1/30 of that under dry sliding. However, as shown above, the total mass loss of both the F and T4-460 alloys after removing corrosion products is a little higher than those under dry sliding. So we can infer that 29/30 mass loss rate is caused by corrosion (~ 0.55 mg/cm²/h for the F alloy and ~ 0.48 mg/cm²/h for the T4-460 alloy). According to the corrosion rate in Fig. 4 by

immersion test, however, the corrosion rate of the F and T4-460 is ~ 0.04 mg/cm²/h and ~ 0.03 mg/cm²/h, respectively, which is an order of magnitude lower than those in SBF with friction and wear. The bright corroded areas on the surfaces of the specimens can be observed from Fig. 9(b) and (d) after immersion in SBF for 60 min. During the wear process, the wear debris is easily to be taken to the surface of the sample, particularly to both ends of the sliding direction. The debris speeds up corrosion rate due to galvanic corrosion, which can be confirmed in Fig. 9(b) and (d). Furthermore, the stainless steel ball, which contacts with the specimen, may also increase the corrosion owing to galvanic corrosion. Therefore, wear accelerates corrosion up to an order of magnitude.

The wear debris morphologies and compositions of the T4-460 alloy collected from specimens under dry sliding and SBF conditions are shown in Fig. 10. The debris after dry sliding in Fig. 10(a) presents various shapes and sizes, and it is rich in Mg and O, with a little Gd and Zn, as shown in Fig. 10(b), indicating oxidation wear mechanism (Ref 41). The size of the debris collected from the specimen tested in SBF is smaller, and its compositions include O, P, Ca, Cl, Na, K from SBF except for the alloying elements. This indicates that the debris was corroded in SBF.

Figure 11 shows the worn tracks of the F and T4-460 under different conditions. In parallel to the direction of the friction, many grooves are presented under dry sliding condition. It indicates that the wear mechanism is abrasive wear. Moreover, some grooves are covered by debris as marked in Fig. 11(a)
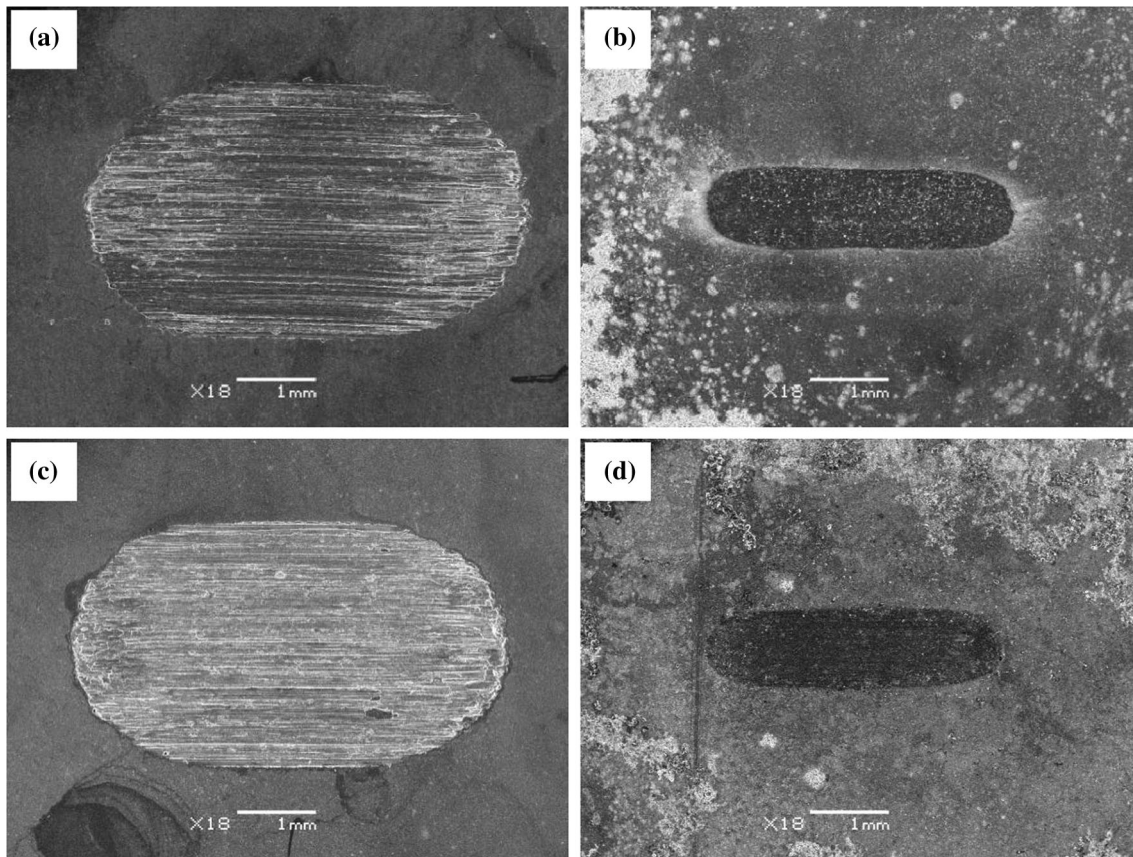
Fig. 9 SEM worn surfaces of the F (a, b) and the T4-460 (c, d) under dry sliding (a, c) and in SBF (b, d) before removing corrosion products

and (c). So it is referred that wear debris is gathered and formed hard particles, causing abrasive wear or plastic deformation wear (Ref 42). In addition, adhesive wear characteristic can also be observed for the dry sliding in Fig. 11(a) and (c). The grooves are much slighter in Fig. 11(b) and (d), which is attributed to the fact that the SBF moves wear debris timely and acts as an effective lubrication. These can explain why the friction coefficient and mass loss caused by wear under dry sliding condition are much higher than those in SBF. Beside the abrasive wear, corrosive wear is also presented because the surface of the worn tracks was corroded by SBF, and the corrosion films were destroyed and moved away by wear.

As mentioned above, after heat treatment, the T4-460 alloy exhibits the lowest mass loss under both dry and SBF sliding conditions. Under dry sliding condition, the T4-460 alloy has the best wear resistance due to the least precipitated phase which reduces the abrasive wear. In SBF, wear obviously accelerates corrosion, and the mass loss is caused by corrosion mostly. With the increase of heat treatment temperature, the wear becomes more severe, which may make corrosion more intense. Consequently, the mass loss of the T4-460 alloy caused by wear is lowest and so is that caused by corrosion. This is responsible for the reason that the trend of total mass loss under dry sliding is similar to that in SBF after removing corrosion products.

4. Conclusions

1. The microstructure of the as-cast GZ62K alloy is mainly composed of α-Mg matrix, $(Mg, Zn)_3Gd$ phase along with the grain boundaries and LPSO structure throughout the matrix grains, and the LPSO structure cannot be observed by SEM after solution treated at the temperature from 460 to 550 °C for 12 h. With increasing the
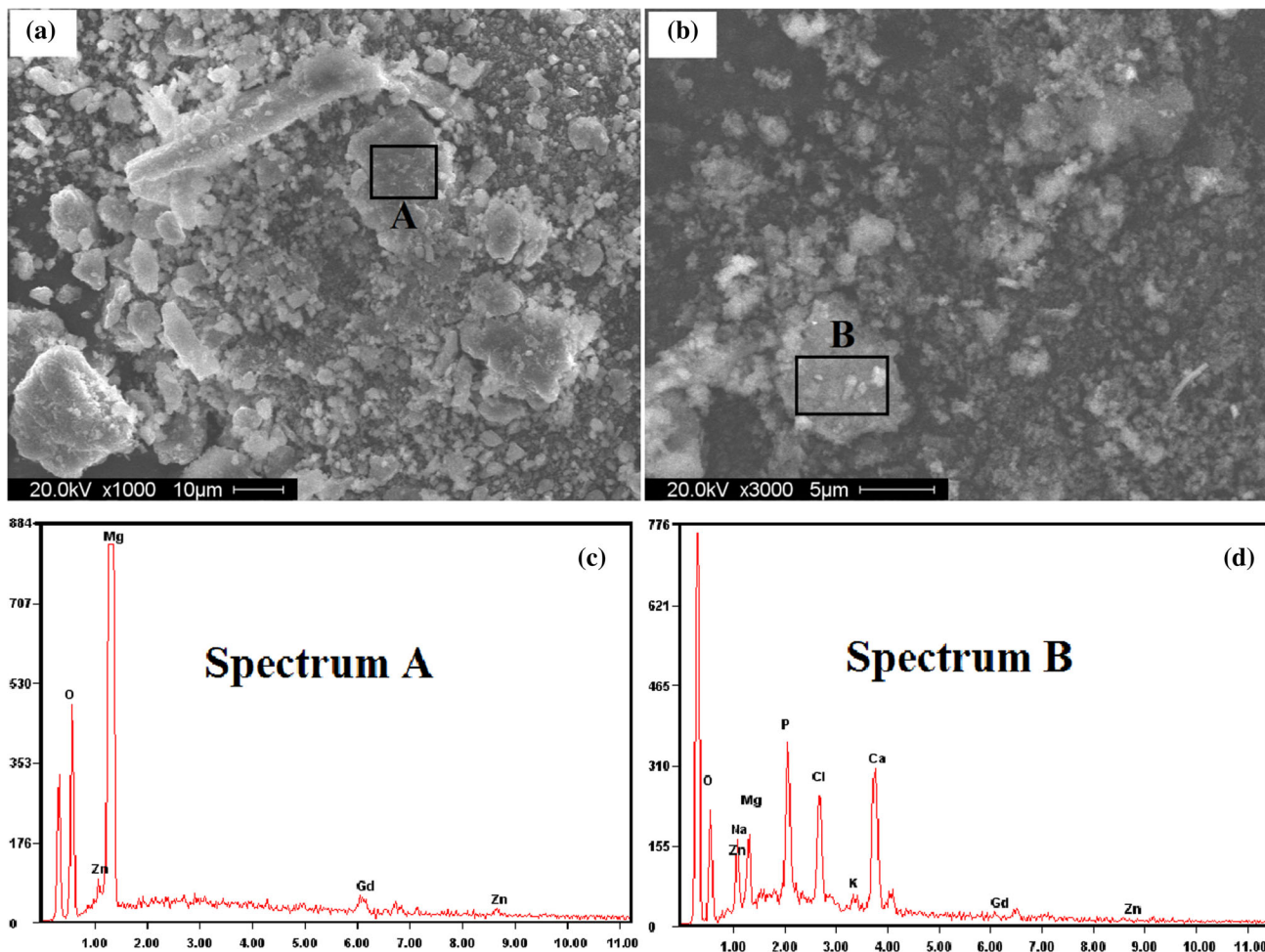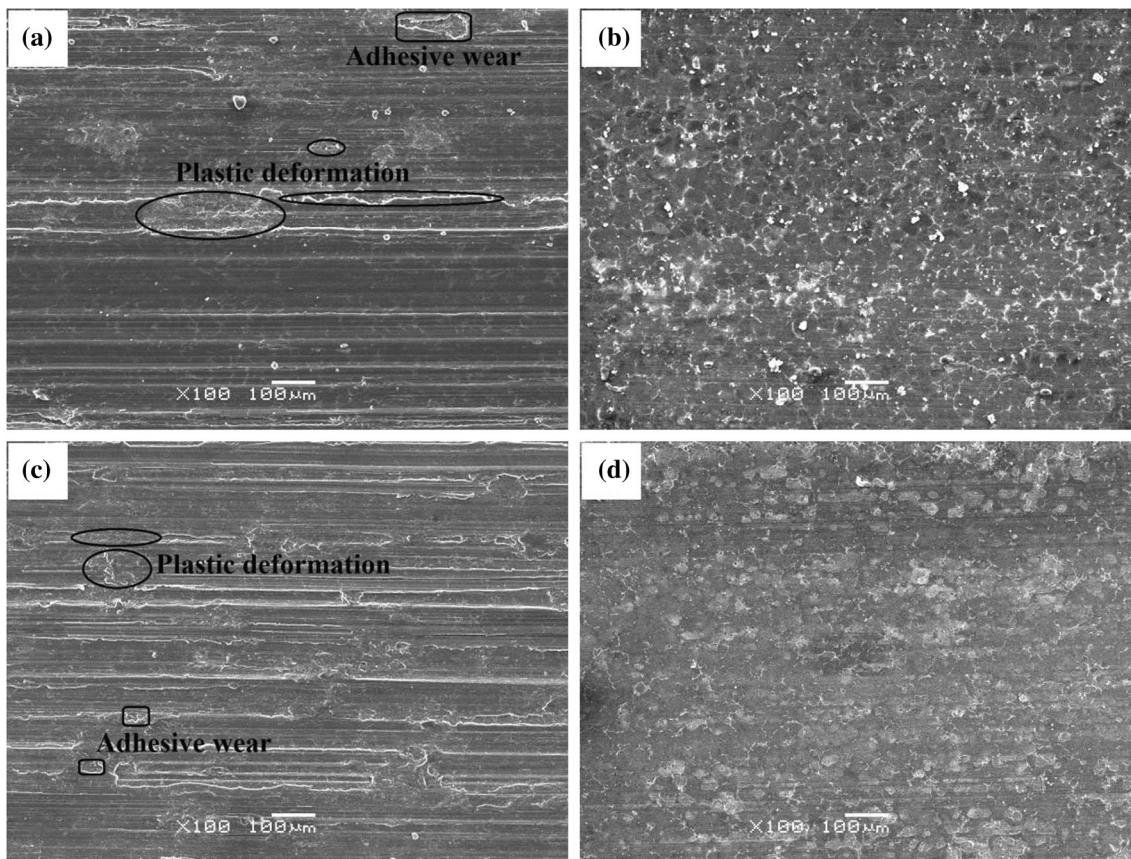
Fig. 10 SEM micrographs of the wear debris of the T4-460 under dry sliding (a) and in SBF (b) and their EDS spectra (c) for area A and (d) for area B

solution temperature, the $(Mg, Zn)_3Gd$ phase decreases and the precipitated phases and hardness gradually increase.

2. The corrosion resistance of the alloy measured by immersion mass loss test is improved from 23 to 44% after solution treatment, and the alloy solution treated at 490 °C exhibits the best corrosion resistance due to the decrease of eutectic phase at grain boundaries.

3. The main wear mechanisms of the alloy under dry sliding are abrasion, adhesion, oxidation and plastic deformation, and those in SBF are mainly abrasion and corrosion.

4. Proper solution treatment can improve wear resistance of the alloy. The alloy solution treated at 460 °C for 12 h presents the lowest mass loss under both dry and SBF sliding conditions due to the least precipitated phase and reduced eutectic phase.

5. Compared with that under dry sliding condition, the friction coefficient and mass loss are significantly reduced in SBF. However, the corrosion is sharply accelerated by wear and dominates the mass loss during friction and wear process in SBF. So not only the corrosion resistance but also the wear resistance of Mg alloys should be improved for bone fixture application.

Fig. 11 SEM worn tracks of the F (a, b) and the T4-460 (c, d) under dry sliding (a, c) and in SBF (b, d) before removing corrosion products

Acknowledgments

References

1. Q.Z. Chen and G.A. Thouas, Metallic Implant Biomaterials, *Mater. Sci. Eng., R*, 2015, **87**, p 1–57
2. M.P. Staiger, A.M. Pietak, J. Huadamai, and G. Dias, Magnesium and it Alloys As Orthopedic Biomaterials: A Review, *Biomaterials*, 2006, **27**, p 1728–1734
3. Y.J. Chen, Z.G. Xu, C. Smith, and J. Sankar, Recent Advances on the Development of Magnesium Alloys for Biodegradable Implants, *Acta Biomater.*, 2014, **10**, p 4561–4573
4. H. Tang, T.Z. Xin, Y. Luo, and F.P. Wang, In Vitro Degradation of AZ31 Magnesium Alloy Coated with Hydroxyapatite by Sol–Gel Method, *Mater. Sci. Technol.*, 2013, **29**, p 547–552
5. W.J. Zhang, M.H. Li, Q. Chen, W.Y. Hu, W.M. Zhang, and W. Xin, Effects of Sr and Sn on Microstructure and Corrosion Resistance of Mg–Zr–Ca Magnesium Alloy for Biomedical Applications, *Mater. Des.*, 2012, **39**, p 379–383
6. D.W. Zhao, F. Witte, F.Q. Lu, J.L. Wang, J.L. Li, and L. Qin, Current Status on Clinical Applications of Magnesium-Based Orthopaedic Implants: A Review from Clinical Translational Perspective, *Biomaterials*, 2017, **112**, p 287–302
7. D. Bose, H. Eggebrecht, M. Haude, A. Schmermund, and R. Erbel, First Absorbable Metal Stent Implantation in Human Coronary Arteries, *Am. Heart Hosp. J.*, 2006, **4**, p 128–130
8. H.R. Bakhsheshi-Rad, E. Hamzah, H.Y. Tok, M. Kasiri-Asgarani, S. Jabbarzare, and M. Medraj, Microstructure, In Vitro Corrosion Behavior and Cytotoxicity of Biodegradable Mg-Ca-Zn and Mg-Ca-Zn-Bi Alloys, *J. Mater. Eng. Perform.*, 2017, **26**, p 653–666
9. Y.F. Zhang, J.K. Xu, Y.C. Ruan, M.K. Yu, M. O'Laughlin, H. Wise, D. Chen, L. Tian, D.F. Shi, J.L. Wang, S.H. Chen, J.Q. Feng, D.H.K. Chow, X.H. Xie, L.Z. Zheng, L. Huang, S. Huang, K. Leung, N. Lu, L. Zhao, H.F. Li, D.W. Zhao, X. Guo, K. Chan, F. Witte, H.C. Chan, Y.F. Zheng, and L. Qin, Implant-Derived Magnesium Induces Local Neuronal Production of CGRP to Improve Bone-Fracture Healing in Rats, *Nat. Med.*, 2016, **22**, p 1160–1169
10. M. Haude, H. Ince, A. Abizaid, R. Toelg, P.A. Lemos, C. Birgelen, E.H. Christiansen, W. Wijns, F.J. Neumann, C. Kaiser, E. Eeckhout, S.T. Lim, J. Escaned, H.M. Garcia-Garcia, and R. Waksman, Safety and Performance of the Second-Generation Drug-Eluting Absorbable Metal Scaffold in Patients with De-Novo Coronary Artery Lesions (BIOSOLVE-II): 6 Month Results of a Prospective, Multicentre, Non-randomised, First-in-Man Trial, *Lancet*, 2016, **387**, p 31–39
11. J.J. Han, P. Wan, Y. Ge, X.M. Fan, L.L. Tan, J.J. Li, and K. Yang, Tailoring the Degradation and Biological Response of a Magnesium–Strontium Alloy for Potential Bone Substitute Application, *Mater. Sci. Eng., C*, 2016, **58**, p 799–811
12. D.W. Zhao, S.B. Huang, F.Q. Lu, B.J. Wang, L. Yang, L. Qin, K. Yang, Y.D. Li, W.R. Li, W. Wang, S.M. Tian, X.Z. Zhang, W.B. Gao, Z.P. Wang, Y. Zhang, X.H. Xie, J.L. Wang, and J.L. Li, Vascularized Bone Grafting Fixed by Biodegradable Magnesium Screw for Treating Osteonecrosis of the Femoral Head, *Biomaterials*, 2016, **81**, p 84–92
13. Z.W. Xie, T. Chen, Q. Chen, Q. Yang, S. Tan, Y.J. Wang, Y.M. Luo, Z.Z. Luo, and M.Q. Hua, Tribocorrosion Behaviors of AlN/MoS₂-Phenolic Resin Duplex Coatings on Nitrogen Implanted Magnesium Alloys, *Surf. Coat. Technol.*, 2015, **266**, p 64–69

14. M.P. Sealy, Y.B. Guo, R.C. Caslaru, J. Sharkins, and D. Feldman, Fatigue Performance of Biodegradable Magnesium-Calcium Alloy Processed by Laser Shock Peening for Orthopedic Implants, *Int. J. Fatigue*, 2016, **82**, p 428–436

15. C. Wan, Z.X. Hao, and S.Z. Wen, Research and Prospect on the Fretting Tribology of the Orthopedic Implants, *Tribology*, 2012, **32**, p 102–109

16. L.J. Cao, Y.J. Wu, L.M. Peng, Q.D. Wang, and W.J. Ding, Microstructure and Tribological Behavior of Mg-Gd-Zn-Zr Alloy with LPSO Structure, *Trans. Nonferrous Met. Soc. China*, 2014, **24**, p 3785–3791

17. J. Zhang, X.B. Zhang, Q.H. Liu, S.J. Yang, and Z.Z. Wang, Effects of Load on Dry Sliding Wear Behavior of Mg-Gd-Zn-Zr Alloys, *J. Mater. Sci. Technol.*, 2017, **33**, p 645–651

18. X.B. Zhang, Q.L. Ma, Z.X. Ba, Z.Z. Wang, and Q. Wang, Microstructure and Corrosion Behaviour in Simulated Body Fluid of Solution Treated Mg-Nd-Gd-Sr-Zn-Zr Alloys, *Rare Met. Mater. Eng.*, 2017, **46**, p 1156–1161

19. X.B. Zhang, Q. Wang, F.B. Chen, Y.J. Wu, Z.Z. Wang, and Q. Wang, Relation Between LPSO Structure and Biocorrosion Behavior of Biodegradable GZ51K Alloy, *Mater. Lett.*, 2015, **138**, p 212–215

20. X.B. Zhang, G.Y. Yuan, X.X. Fang, Z.Z. Wang, and T. Zhang, Effects of Solution Treatment on Yield Ratio and Biocorrosion Behaviour of As-Extruded Mg-2.7Nd-0.2Zn-0.4Zr Alloy for Cardiovascular Stent Application, *Mater. Technol.*, 2013, **28**, p 155–158

21. K. Chen, J.W. Dai, and X.B. Zhang, Improvement of Corrosion Resistance of Magnesium Alloys for Biomedical Applications, *Corros. Rev.*, 2015, **33**, p 101–117

22. X.B. Zhang, Y.J. Wu, Y.J. Xue, Z.Z. Wang, and L. Yang, Biocorrosion Behavior and Cytotoxicity of a Mg-Gd-Zn-Zr Alloy with Long Period Stacking Ordered Structure, *Mater. Lett.*, 2012, **86**, p 42–45

23. F. Feyerabend, J. Fischer, J. Holtz, F. Witte, R. Willumeit, H. Drücker, C. Vogt, and N. Hort, Evaluation of Short-Term Effects of Rare Earth and Other Elements Used in Magnesium Alloys on Primary Cells and Cell Lines, *Acta Biomater.*, 2010, **6**, p 1834–1842

24. S.X. Zhang, X.N. Zhang, C.L. Zhao, J.N. Li, Y. Song, C.Y. Xie, H.R. Tao, Y. Zhang, Y.H. He, Y. Jiang, and Y.J. Bian, Research on an Mg-Zn Alloy as a Degradable Biomaterial, *Acta Biomater.*, 2010, **6**, p 626–640

25. X.Y. Ye, M.F. Chen, M. Yang, J. Wei, and D.B. Liu, In Vitro Corrosion Resistance and Cytocompatibility of Nano-Hydroxyapatite Reinforced Mg-Zn-Zr Composites, *J. Mater. Sci. Mater. Med.*, 2010, **21**, p 1321–1328

26. X.B. Zhang, Z.X. Ba, Z.Z. Wang, and Y.J. Xue, Microstructures and Corrosion Behavior of Biodegradable Mg-6Gd-xZn-0.4Zr Alloys with and Without Long Period Stacking Ordered Structure, *Corros. Sci.*, 2016, **105**, p 68–77

27. X.B. Zhang, Q. Wang, Z.X. Ba, Z.Z. Wang, and Y.J. Xue, Improved Corrosion Resistance of As-Extruded GZ51K Biomagnesium Alloy with High Mechanical Properties by Aging Treatment, *J. Mater. Eng. Perform.*, 2016, **25**, p 719–725

28. W. Rong, Y. Zhang, Y.J. Wu, M. Sun, J. Chen, Y. Wang, J.Y. Han, L.M. Peng, and H.X. Ding, Effects of Zr and Mn Additions on Formation of LPSO Structure and Dynamic Recrystallization Behavior of Mg-15Gd-1Zn Alloy, *J. Alloy. Compd.*, 2017, **692**, p 805–816

29. Y.X. Du, Y.J. Wu, L.M. Peng, J. Chen, X.Q. Zeng, and W.J. Ding, Formation of Lamellar Phase with 18R-type LPSO Structure in an As-Cast Mg96Gd3Zn1 (at%) Alloy, *Mater. Lett.*, 2016, **169**, p 168–171

30. K. Gusieva, C.H.J. Davies, J.R. Scully, and N. Birbilis, Corrosion of Magnesium Alloys: The Role of Alloying, *Int. Mater. Rev.*, 2015, **60**, p 169–194

31. L.G. Bland, N. Birbilis, and J.R. Scully, Exploring the Effects of Intermetallic Particle Size and Spacing on the Corrosion of Mg-Al Alloys Using Model Electrodes, *J. Electrochem. Soc.*, 2016, **163**, p C895–C906

32. C.Q. Li, D.K. Xu, Z.R. Zeng, B.J. Wang, L.Y. Wang, X.B. Chen, and E.H. Han, Effect of Volume Fraction of LPSO Phases on Corrosion and Mechanical Properties of Mg-Zn-Y Alloys, *Mater. Des.*, 2017, **121**, p 430–441

33. J.J. Han, P. Wan, Y. Sun, Z.Y. Liu, X.M. Fan, L.L. Tan, and K. Yang, Fabrication and Evaluation of a Bioactive Sr-Ca-P Contained Micro-arc Oxidation Coating on Magnesium Strontium Alloy for Bone Repair Application, *J. Mater. Sci. Technol.*, 2016, **32**, p 233–244

34. X.B. Zhang, Z.X. Ba, Z.Z. Wang, Y.J. Xue, and Q. Wang, Microstructure and Biocorrosion Behaviors of Solution Treated and As-Extruded Mg-2.2Nd-xSr-0.3Zr Alloys, *Trans. Nonferrous Met. Soc. China*, 2014, **24**, p 3793–3803

35. Z.M. Shi, M. Liu, and A. Atrens, Measurement of the Corrosion Rate of Magnesium Alloys Using Tafel Extrapolation, *Corros. Sci.*, 2010, **52**, p 579–588

36. J.S. Zhang, D. Wang, W.B. Zhang, H.X. Pei, Z.Y. You, C.X. Xu, and W.L. Cheng, The relation Between Microstructure and Corrosion Behavior of Mg–Gd–Zn Alloy with Long Period Stacking Ordered Structure, *Mater. Corros.*, 2015, **66**, p 542–548

37. X.B. Zhang, Z.X. Ba, Q. Wang, Y.J. Wu, Z.Z. Wang, and Q. Wang, Uniform Corrosion Behavior of GZ51K Alloy with Long Period Stacking Ordered Structure for Biomedical Application, *Corros. Sci.*, 2014, **88**, p 1–5

38. A. Srinivasan, Y. Huang, C.L. Mendis, C. Blawert, K.U. Kainer, and N. Hort, Investigations on Microstructures, Mechanical and Corrosion Properties of Mg–Gd–Zn Alloys, *Mater. Sci. Eng., A*, 2014, **595**, p 224–234

39. D.B. Liu, B. Wu, X. Wang, and M.F. Chen, Corrosion and Wear Behavior of an Mg–2Zn–0.2Mn Alloy in Simulated Body Fluid, *Rare Met.*, 2015, **34**, p 553–559

40. H. Li, D.B. Liu, Y. Zhao, F. Jin, and M.F. Chen, The Influence of Zn Content on the Corrosion and Wear Performance of Mg-Zn-Ca Alloy in Simulated Body Fluid, *J. Mater. Eng. Perform.*, 2016, **25**, p 3890–3895

41. S.W. Xia, Y. Liu, D.M. Fu, B. Jin, and J. Lu, Effect of Surface Mechanical Attrition Treatment on Tribological Behavior of the AZ31 Alloy, *J. Mater. Sci. Technol.*, 2016, **32**, p 1245–1251

42. J. An, X.H. Xuan, J. Zhao, W. Sun, and C. Liang, Dry Sliding Wear Behavior and Subsurface Microstructure Evolution of Mg97Zn1Y2 Alloy in a Wide Sliding Speed Range, *J. Mater. Eng. Perform.*, 2016, **25**, p 5363–5373